JOURNAL OF THERMOPHYSICS AND HEAT TRANSFER
Vol. 24, No. 3, July–September 2010

Numerical Investigation of the Radiative Properties of Polymeric Foams from Tomographic Images

R. Coquard*
Etude Conseils Calcul en Mécanique des Structures, 69603 Villeurbanne Cedex, France
D. Baillis†
Centre Thermique de Lyon, 69621 Villeurbanne Cedex, France
and
E. Maire‡
Centre National de la Recherche Scientifique, 69621 Villeurbanne Cedex, France

DOI: 10.2514/1.46988

Polymeric closed-cell foams are widely used in various applications where their insulating performance is of interest. In most of these applications, radiation propagation is an important mode of heat transfer. That is the reason why many studies have already been performed in the prediction of the radiative behavior. Until now, these studies were based on ideal representations of the cellular structure that simplify the real porous morphology. However, the recent development of x-ray tomography allows envisaging a noticeable improvement in the morphological characterization of these materials, which can be used to achieve a better numerical estimation of their radiative properties. To fulfill this objective, a numerical method for computing the directional radiative properties of particulate media based on ray-tracing procedures has been developed. The method to three-dimensional binary representations of the cellular structures obtained from x-ray tomography on plastic foams has been applied. The comparison between the spectral radiative properties computed by the simplified models of the literature and by our original models permits us to determine which assumptions are the most detrimental to the reliability of the simplified models.

Nomenclature

$\boldsymbol{A_p}$	=	total absorbance of the cell window
$\boldsymbol{D}_{\text{cell}}$	=	cell diameter, m
$\langle \boldsymbol{D}_{\text{cell}} \rangle$	=	mean cell diameter, m
$\boldsymbol{D}_{\text{cell,sphere}}$	=	spherical equivalent cell diameter, m
$D_\lambda(\theta_i)$	=	mean angular repartition of the radiative energy scattered by the solid phase in volumetric approach
$D'_\lambda(\theta_i)$	=	mean angular repartition of the radiative energy scattered by the solid phase in shell-mesh approach
$\boldsymbol{d\Omega}(\theta_i)$	=	solid angle around direction θ_i, sr
$E(\theta')$	=	mean angular repartition of the rays impacting the solid phase
$\boldsymbol{g}$	=	global asymmetry factor of the phase function
$\boldsymbol{g}_\lambda$	=	spectral asymmetry factor of the phase function
$\boldsymbol{h}$	=	thickness of the cell windows, m
$\boldsymbol{I}_\lambda(z, \boldsymbol{\Delta})$	=	spectral radiant intensity at location z in direction $\boldsymbol{\Delta}$, $\mathrm{W/m^2/Sr}$
$\boldsymbol{I}^0_\lambda(\boldsymbol{T})$	=	spectral radiant intensity of a black body at temperature T, $\mathrm{W/m^2/Sr}$
$\boldsymbol{k}_\lambda$	=	imaginary part of the refractive index of the polymer
$\boldsymbol{l}$	=	distance traveled by the rays in polymer, m
$\boldsymbol{l}_{\text{mean}}$	=	mean free path of rays in the material, m
$\boldsymbol{N}$	=	number of rays thrown during the ray-tracing procedure
N_{cell}	=	number of cells contained in the foam sample
$\boldsymbol{n}_\lambda$	=	real part of the refractive index of the polymer
$\tilde{\boldsymbol{n}}_\lambda = \boldsymbol{n}_\lambda - \boldsymbol{i}\boldsymbol{k}_\lambda$	=	complex spectral refractive index of the polymer
$\boldsymbol{P}(\boldsymbol{\Delta} \to \boldsymbol{\Delta}') = \boldsymbol{P}(\theta)$	=	global scattering phase function
$\boldsymbol{P}_\lambda(\boldsymbol{\Delta} \to \boldsymbol{\Delta}') = \boldsymbol{P}_\lambda(\theta)$	=	spectral scattering phase function
$\boldsymbol{R_p}$	=	total reflectance of the cell window
$\boldsymbol{R}_{12}$	=	reflectivity of the interface between air (1) and polymer (2)
$\boldsymbol{R}_{21}$	=	reflectivity of the interface between polymer (2) and air (1)
T	=	temperature, K
$\boldsymbol{T_p}$	=	total transmittance of the cell window
$\boldsymbol{T_r}$	=	transmittivity of the polymer layer
$\boldsymbol{T}_{12}$	=	transmittivity of the interface between air (1) and polymer (2)
$\boldsymbol{T}_{21}$	=	transmittivity of the interface between polymer (2) and air (1)
$\boldsymbol{V}$	=	volume, $\mathrm{m^3}$
Z	=	one-dimensional coordinate, m
β	=	global extinction coefficient, $\mathrm{m^{-1}}$
β_λ	=	spectral extinction coefficient, $\mathrm{m^{-1}}$
β^*_λ	=	weighted spectral extinction coefficient, $\mathrm{m^{-1}}$
β^*	=	weighted global extinction coefficient, $\mathrm{m^{-1}}$
$\boldsymbol{\Delta}$	=	incident direction vector
$\boldsymbol{\Delta}'$	=	scattering direction vector
ε	=	porosity of the foam sample
ε_{CV}	=	porosity of the cubic volumes
θ	=	angle between incident and scattering directions, rad
θ_{inc}	=	angle of incidence, rad

Received 2 September 2009; revision received 8 March 2010; accepted for publication 9 March 2010.

*66, Boulevard Niels Bohr; remi.coquard@ec2-ms.fr.
†Unité Mixte de Recherche, 5008, Domaine Scientifique de la Doua; also Institut National des Sciences Appliquées de Lyon, Bâtiment Sadi Carnot, 9 rue de la Physique, F-69300 Villeurbanne France; dominique.baillis@insa-lyon.fr.
‡Materials Engineering and Science Laboratory, Domaine Scientifique de la Doua, Bâtiment Antoine de Saint-Exupery, 25 Avenue Jean Capelle; Eric.Maire@insa-lyon.fr.

θ_{ref}	=	angle of reflection, rad
θ_{refr}	=	angle of refraction, rad
θ_{sca}	=	angle between incident and scattering direction, rad
θ'	=	angle between the rays and the normal to the surface elements impacted, rad
θ''	=	angle between the starting direction and the outward normal of the element, rad
κ	=	global absorption coefficient, m^{-1}
κ_λ	=	spectral absorption coefficient, m^{-1}
λ	=	radiation wavelength, μm
$\mu = \cos(\theta)$	=	direction cosine
ξ	=	randomly generated number ranging between 0 and 1
σ	=	global scattering coefficient, m^{-1}
$\sigma_{D\text{cell}}$	=	standard deviation of cell diameter, m
σ_λ	=	spectral scattering coefficient, m^{-1}
σ_λ^*	=	weighted spectral scattering coefficient, m^{-1}
σ^*	=	weighted global scattering coefficient, m^{-1}
Ω	=	solid angle, sr
$\omega_\lambda = \sigma_\lambda/\beta_\lambda$	=	spectral scattering albedo

Subscripts

abs	=	absorbed
av1	=	arithmetic averaging
av2	=	averaging weighted by the volume of each cell
i	=	of the ith cell contained in foam sample
inc	=	incident
max	=	maximum values
min	=	minimum values
random	=	in random directions
ref	=	reflected
refr	=	refracted
SM	=	using shell-mesh approach
sca	=	scattered
t	=	transmitted
VM	=	using volumetric mesh approach
X	=	in X direction
Y	=	in Y direction
Z	=	in Z direction
λ	=	spectral value

I. Introduction

HIGH-POROSITY foams are widely used in numerous applications for thermal insulation due to their low equivalent thermal conductivities. Depending on the domain of application, the solid matrix can be made of metals, ceramics, or polymers. Although similar, the porous structure of metal–ceramic foams and polymeric foams can differ significantly. Indeed, metal/ceramic foams exhibit an open-cell structure with porosities ranging from 0.8 to 0.95, whereas polymeric cellular materials can either be open or closed and have a higher porosity. For applications requiring light weight and high-insulating efficiencies at ambient temperatures, polymeric foams, such as polyurethane (PU) or polystyrene [extruded and expanded (EPS)] foams are typically used, notably for the thermal insulation of buildings.

Given the very high porosity of these materials, the total heat transfer in polymeric foams is due to both conduction and thermal radiation. As a consequence, a large number of studies has been conducted in the theoretical characterization of radiative transfer in this type of porous media. Glicksmann and Scheutz [1] were the first to conduct a general study on radiative transfer by assimilating polymer foams into random arrangements of opaque struts with triangular cross sections and partially transparent windows under an independent scattering hypothesis. The authors proposed an expression for the scaled extinction coefficient depending on the cell diameter and porosity of the foam. Subsequently, Kuhn et al. [2,3] proposed a similar approach for plastic foams and modeled the porous structure by dodecahedral cells composed of cylindrical struts and pentagonal windows. These studies were especially interested in plastic foams with relatively high densities, and the theoretical results did not show good agreement with experimental measurements for foams with relatively low densities. This could be explained by the fact that the authors had recourse to only one parameter to take into account the radiative heat transfer, the weighted Rosseland extinction coefficient, whereas the entire set of radiative properties is required for very low densities. Recently, Coquard and Baillis [4] and Coquard et al. [5] have been interested more specifically in the radiative properties of EPS. Their model is based on a detailed representation of the complex morphology of EPS foams. They computed the spectral extinction coefficient, scattering albedo and scattering phase function for varying cell shapes and porosities using the refractive index of polystyrene identified from spectrometric measurements on thin sections of polystyrene. For several foam samples, the complete model was validated by comparing the spectral hemispherical reflectance and transmittance measurements with predicted values.

All of these models were developed assuming idealized homogeneous cellular structures, composed of simplified identical particles, or structures which can be represented by a unique representative cell. This constitutes the main deficiency of these models since the porous structure of real high-porosity foams is composed of cells with irregular shapes and sizes in which the solid phase is not distributed homogeneously. Moreover, it is always assumed that independent scattering occurs even though the particles forming the foam might be located next to each other. That is the reason why, during the last few years, there has been a growing interest in a tomography-based model. Such models theoretically permit one to account for the exact morphology of the porous structure. Loretz et al. [6] used x-ray tomography to analyze the porous structure and estimate the values of the structural parameters of aluminum foams. However, Zeghondy et al. [7,8] were the first to directly apply a radiative properties computation to the representation of the porous structure obtained by x-ray tomography. They applied radiative distribution function identification (RDFI), originally proposed by Tancrez and Taine [9], to a tomographic representation of open-cell mullite foams. They validated their approach by comparing experimentally measured reflectance to that predicted for a homogeneous semitransparent material whose anisotropic radiative properties were obtained by RDFI. Good agreement was found. Shortly after, Rousseau et al. [10] applied a Monte Carlo ray-tracing technique to slabs of porous silica glass reconstructed from x-ray tomography. They computed the normal hemispherical spectral reflectance and transmittance of the slab and thus its emittance. However, their procedure did not allow computing the radiative properties of the equivalent homogeneous semitransparent material. Just about the same time, Petrasch et al. [11] applied another Monte Carlo ray-tracing procedure to reticulate porous ceramics to calculate the extinction coefficients and scattering phase functions based on the newly developed probabilistic distribution functions of the extinction path length and of the directional cosine of the incident radiation. The authors took into account purely diffuse or perfectly specular surfaces. They showed that the extinction coefficient is directionally independent, justifying the isotropic assumption.

These first studies, conducted using tomographic representations for the computation of the radiative behavior of high-porosity foams, are promising, as they permit one to improve the prediction of the radiative heat transfer in various materials for which experimental investigation is difficult. However, the studies have never been applied to foams for which the solid phase is nonopaque to radiation. Moreover, they do not permit evaluation and highlighting of the improvements brought about by the use of tomography in comparison with previous classical models.

Consequently, we have developed an improved model for evaluation of the spectral radiative properties of closed-cellular materials from the three-dimensional (3-D) representation obtained by x-ray tomography. This method allows evaluation of the directional radiative properties and has been applied to several samples of high-porosity closed-cell foams. The comparison of the results obtained with simpler models based on ideal representation of

the porous structures would permit underscoring the main deficiencies of current simplified models and the advances brought about by x-ray tomography.

II. Radiative Transfer in Foams: A Summary

Radiative heat transfer in a low-density porous medium is a relatively complex problem given that it takes into account the emission, absorption and also scattering of radiation by the porous material. This radiative behavior may also vary with the radiation wavelength λ considered. The propagation of radiation in these materials is generally treated by regarding them as homogeneous semitransparent materials characterized by three spectral radiative properties:

1) The first property is the monochromatic extinction coefficient β_λ (m^{-1}), inversely proportional to the mean free path of a photon in the medium before extinction.

2) The second property is the monochromatic scattering albedo, $\omega_\lambda = \sigma_\lambda/\beta_\lambda$, representing the proportion of the attenuated energy that is scattered out of the direction of interest.

3) The third property is the scattering phase function, $\boldsymbol{P}_\lambda(\boldsymbol{\Delta}' \rightarrow \boldsymbol{\Delta})$, describing the angular distribution of the energy scattered by the medium and which simplifies to $\boldsymbol{P}_\lambda(\theta)$ when considering azimuthal symmetry; θ being the angle between the incident and scattered directions.

Radiative transfer in the material is then governed by the radiative transfer equation (RTE), which is well described in standard textbooks [12–14]:

$$\frac{\mu}{\beta_\lambda}\frac{\partial \boldsymbol{I}_\lambda(z,\boldsymbol{\Delta})}{\partial z} + \boldsymbol{I}_\lambda(z,\boldsymbol{\Delta}) = (1-\omega_\lambda)\boldsymbol{I}^0_\lambda(\boldsymbol{T}) + \frac{\omega_\lambda}{2}\int_0^\pi \boldsymbol{P}_\lambda(\boldsymbol{\Delta}' \rightarrow \boldsymbol{\Delta})\boldsymbol{I}_\lambda(z,\boldsymbol{\Delta}')\,\mathbf{d}\mu' \quad (1)$$

Several other characteristics derived from β_λ, ω_λ, and $P_\lambda(\theta)$ are usually considered:

1) The asymmetry parameter,

$$\boldsymbol{g}_\lambda = \frac{1}{4\pi}\int_{\boldsymbol{\Omega}=4\pi} \boldsymbol{P}_\lambda(\boldsymbol{\Delta}' \rightarrow \boldsymbol{\Delta})\cos\theta\,\mathbf{d}\boldsymbol{\Omega} = 0.5\int_0^\pi \boldsymbol{P}_\lambda(\theta)\cos\theta\sin\theta\,\mathbf{d}\theta \quad (2)$$

which describes the way the energy is scattered: $0 < g < 1$ means that the radiation is predominantly scattered in forward directions, whereas $-1 < g < 0$ means that the radiation is predominantly scattered in backward directions.

2) The weighted scattering and extinction coefficients,

$$\sigma^*_\lambda = \sigma_\lambda(1-\boldsymbol{g}_\lambda); \qquad \beta^*_\lambda = \kappa_\lambda + \sigma_\lambda(1-\boldsymbol{g}_\lambda) = \kappa_\lambda + \sigma^*_\lambda \quad (3)$$

Contrary to σ_λ, σ^*_λ not only quantifies the probability of an intercepted ray being scattered but encompasses the whole scattering phenomenon by taking into account the way the radiative energy is redistributed via the asymmetry factor g_λ.

3) The global radiative properties β, σ, κ, and $\boldsymbol{P}(\theta)$, which summarize the spectral variation of the radiative properties $\beta_\lambda, \sigma_\lambda, \kappa_\lambda$, and $\boldsymbol{P}_\lambda(\theta)$ by integrating them over the whole wavelength spectrum using the blackbody emission function:

$$\beta = \frac{\int_0^\infty \beta_\lambda \boldsymbol{I}^0_\lambda(\boldsymbol{T})\,\mathbf{d}\lambda}{\int_0^\infty \boldsymbol{I}^0_\lambda(\boldsymbol{T})\,\mathbf{d}\lambda}; \qquad \sigma = \frac{\int_0^\infty \sigma_\lambda \boldsymbol{I}^0_\lambda(\boldsymbol{T})\,\mathbf{d}\lambda}{\int_0^\infty \boldsymbol{I}^0_\lambda(\boldsymbol{T})\,\mathbf{d}\lambda}$$

$$\boldsymbol{P}(\theta) = \frac{\int_0^\infty \boldsymbol{P}_\lambda(\theta)\boldsymbol{I}^0_\lambda(\boldsymbol{T})\,\mathbf{d}\lambda}{\int_0^\infty \boldsymbol{I}^0_\lambda(\boldsymbol{T})\,\mathbf{d}\lambda}; \qquad \boldsymbol{g} = \frac{\int_0^\pi \boldsymbol{P}(\theta)\cos\theta\sin\theta\,\mathbf{d}\theta}{2} \quad (4)$$

The radiative properties of an equivalent homogeneous semitransparent material are closely related to the properties of the constituents of the dispersed materials and to the morphology of the porous structure. As explained in the Introduction, several researchers [1–5] have proposed theoretical models for the prediction of the complex radiative properties of polymeric foams. They are based on ideal representations of the porous structure.

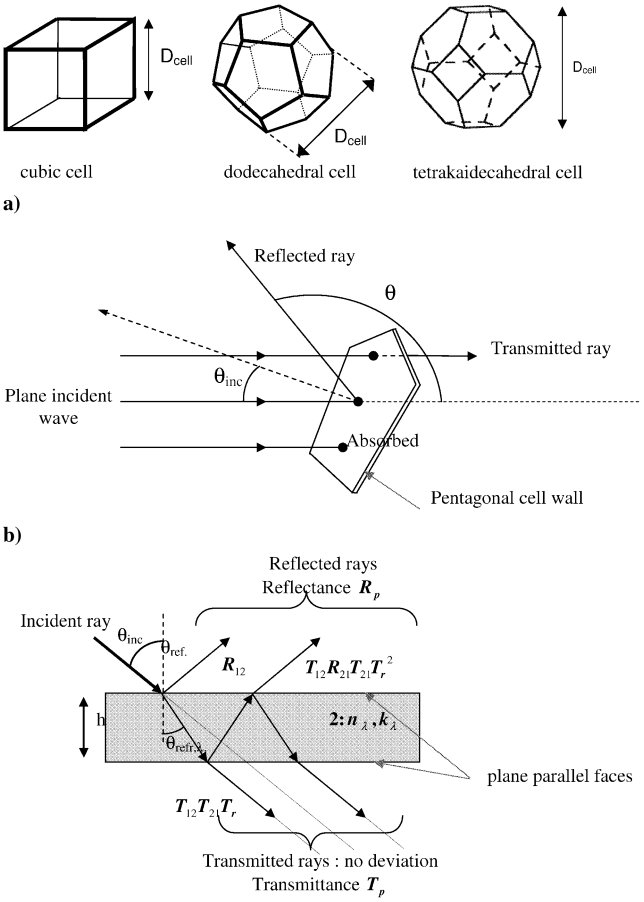

Fig. 1 Illustration of the computational model of the radiative properties from [5].

For high-porosity closed-cell polymeric foams, the most sophisticated general model has been developed by Coquard et al. [5] for the cellular material contained in beads of EPS foam. The authors considered porous material composed of cubic, dodecahedral, or tetrakaidecahedral cells (see Fig. 1a) in which all of the solid phase is present in the cell walls (i.e., the amount of matter at the vertices of the cells was assumed to be negligible). They also considered the cell walls to be plane parallel, with a constant thickness throughout the entire porous volume. They treated the interaction of radiation with the cellular structure by assimilating it into a random dispersion of cell walls randomly oriented, which scatter radiation independently. For cellular materials made of cubic cells, square walls with constant thickness were considered, whereas pentagonal windows and hexagonal/square windows were considered for dodecahedral and tetrakaidecahedral cells, respectively. Under the independent scattering hypothesis, the radiative properties were obtained simply by summing up the individual contributions of all of the walls present in a unit volume. The number of particles per unit volume as well as the thickness of the walls was related simply to the porosity and the cell diameter of the medium, depending upon the shapes of the cells considered (cubic, dodecahedral, and tetrakaidecahedral). The radiative characteristics of the particles (square, pentagonal, or hexagonal windows) were computed by analyzing the interaction of a plane incident wave with a randomly oriented plane-parallel particle (see Fig. 1b). To do that, they used a geometric optics approximation, since the cell diameter, and thus the dimensions of the cell walls, were much greater than the radiation wavelength considered. The reflectance R_p, absorbance A_p, and transmittance $\boldsymbol{T}_p$ of the windows (see Fig. 1c) can be computed from the cell wall thickness h, the incident angle of radiation, and the optical properties of the solid phase:

$$\left.\begin{aligned} \boldsymbol{R}_p &= \boldsymbol{R}_{12} + \boldsymbol{T}_{12}\boldsymbol{R}_{21}\boldsymbol{T}_{21}\boldsymbol{T}_r^2 + \boldsymbol{T}_{12}\boldsymbol{R}_{21}^3\boldsymbol{T}_{21}\boldsymbol{T}_r^4 + \cdots = \boldsymbol{R}_{12} + \frac{\boldsymbol{T}_{12}\boldsymbol{R}_{21}\boldsymbol{T}_{21}\boldsymbol{T}_r^2}{1-\boldsymbol{R}_{21}^2\boldsymbol{T}_r^2} \\ \boldsymbol{T}_p &= \boldsymbol{T}_{12}\boldsymbol{T}_{21}\boldsymbol{T}_r + \boldsymbol{T}_{12}\boldsymbol{R}_{21}^2\boldsymbol{T}_{21}\boldsymbol{T}_r^3 + \cdots = \frac{\boldsymbol{T}_{12}\boldsymbol{T}_{21}\boldsymbol{T}_r}{1-\boldsymbol{R}_{21}^2\boldsymbol{T}_r^2} \quad \text{and} \quad \boldsymbol{A}_p = 1 - \boldsymbol{R}_p - \boldsymbol{T}_p \\ \text{with} \quad \boldsymbol{T}_r &= \exp\left(-\frac{4\pi\boldsymbol{k}_\lambda \boldsymbol{h}}{\lambda\cos(\theta_{\text{refr},\lambda})}\right); \qquad \boldsymbol{n}_\lambda \sin(\theta_{\text{refr},\lambda}) = \sin(\theta_{\text{inc}}) \end{aligned}\right\} \quad (5)$$

and $\boldsymbol{R}_{12}$, $\boldsymbol{T}_{12}$, $\boldsymbol{R}_{21}$, and $\boldsymbol{T}_{21}$ are given by Fresnel's relations detailed in standard textbooks [12–14].

The radiative properties of the cellular materials were then computed assuming a homogeneous cell size, corresponding generally to the mean cell size of the sample considered.

III. Description of Model

We have developed an original numerical method allowing computation of the equivalent spectral radiative properties of a porous material from the 3-D representation of its structure and the optical properties of the solid material, i.e., the refractive indexes. It has been applied to the representation of the structure of polymeric foams obtained by x-ray tomography. The numerical method is close to that proposed by Randrianalisoa and Baillis for the radiative behavior of dispersed media [15] and densely packed spheres in semitransparent media [16]. The method is based on ray-tracing procedures assuming that the radiation-matter interaction in the medium could be treated by means of geometric optics laws at the local scale and that no diffraction effect occurs. These hypotheses are acceptable only if the dimensions of the particles encountered during the ray tracing are far larger than the radiation wavelengths considered for the radiative heat transfer. At ambient temperatures, most of the radiative heat transfer occurs for radiation wavelengths near 10 μm. Thus, ray tracing is applicable to porous materials composed of particles with characteristic dimensions greater than a few tens of μm, which is the case for open-cell polymeric foams with cell diameters of several hundreds of micrometers. Moreover, the fluid phase, which is air, is assumed to be transparent. In this first section, in order to simplify the description of the method, we will also assume that the radiative behavior of the porous material could be approximated by an isotropic semitransparent material. Numerical investigations concerning the anisotropy of the porous materials will be discussed next.

A. Porous Structure Meshing from X-Ray Tomography

The tomographic representations of the different foams analyzed have been obtained using two different tomographs: the microx-ray tomograph of the Materials Engineering and Science (MATEIS) Laboratory of Institut National des Sciences Appliquées de Lyon (INSA), and the high resolution x-ray tomograph of the European Synchrotron Radiation Facility (ESRF) (beam line identification 19) in Grenoble, France. The best resolution of the ESRF tomograph is 0.4 μm and only several micrometers for the MATEIS tomograph. The data acquisition was done by the MATEIS team [17].

The 3-D tomographic images come in the form of voluminous RAW files containing the gray scales of the cubic voxels forming a parallelepipedic piece of foam sample. The raw images extracted from the tomographs (either the MATEIS or the ID 19 ESRF tomograph) were first reconstructed. In each case, we used a Feldkampf classical algorithm commercially provided for the MATEIS tomograph and available for the users in the case of the ESRF. During reconstruction, each of the software packages used allowed for ring artefact reduction and eventual correction of the motion of the sample. Once reconstructed, the raw data were median filtered and binarized (simply thresholded in the case of the MATEIS based images, and using a region growing segmentation because of the phase contrast in the ESRF images). The thresholding was conducted so that the proportion of void voxels fit the porosity determined experimentally. All of these operations were performed using ImageJ freeware. The choice of voxel size (the resolution) is a key issue, since it should be sufficiently small to reconstruct faithfully the smallest particles composing the porous structure but should also be large enough so that the analyzed sample contains a sufficient amount of particles. In Figs. 2a and 2b, we have presented tomographic slices from polyvinyl chloride (PVC) foam before and after filtering and binarization. Actually, there remain some inaccuracies after the thresholding/segmentation but they are sufficiently rare so that the radiative properties are not affected significantly.

The large size of the data to process required the use of a dedicated desktop computer. All of the image processing calculations were performed on a 16 GB double-data random access memory, 64-bit dual-core dual-processor desktop computer operated using the Linux operating system. The typical processing time (mainly CPU time) for treating a 1 GB data set was between 1 to 5 h. The image treatment plug-ins used could potentially be rewritten in a way using the multiprocessor capability of ImageJ (this could potentially speed up the processes by a factor of 4 to 8), but this was out of the scope of the present study.

For the Monte Carlo ray-tracing procedure, a geometrical representation of the porous structure, showing the interface between solid and fluid phases, is required rather than a 3-D volumetric grid. To obtain this suitable surface representation from the 3-D volumetric grid, we used a procedure described by Youssef et al. [18]. This procedure is based on the routines implemented in the Amira software, which has a special instruction called SurfaceGen. This instruction allows meshing the surface to show the solid–fluid interface using triangular surface elements based on a marching cube smoothing of this voxelized surface. A 3-D rendering of the volumetric surface mesh obtained from the tomographic images depicted on Figs. 2a and 2b is illustrated on Fig. 2c. Generally, the number of surface elements generated is huge, and simplification of the surface mesh is required.

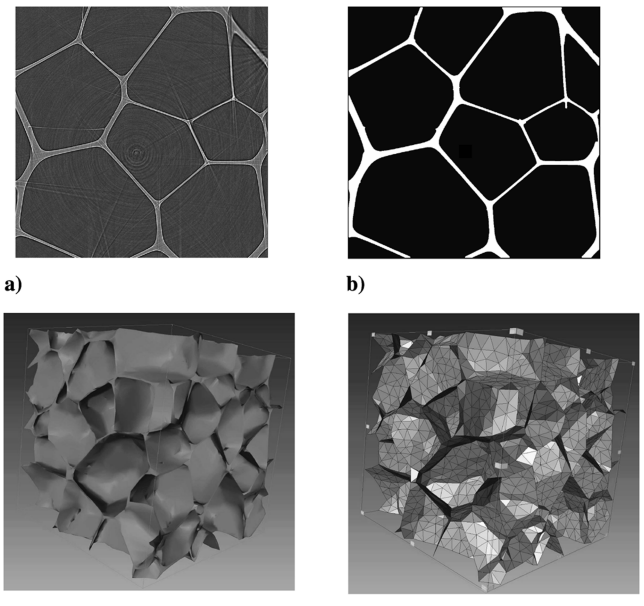

Fig. 2 Illustration of ray tracing for the shell-mesh and volumetric mesh approaches.

For high-porosity closed-cell foams (PVC or polystyrene foams), the faces of cells separating neighboring pores are very thin, and the amount of matter present at the edge (forming the so-called cell struts) is almost negligible. In this case, it was very interesting to use another type of surface mesh, called shell surface mesh, demarcating the borderline between neighboring cells. To do this, we used a method already presented in [19]. This method is based on the skeletonization of the solid phase by thinning down. The final goal is to determine, by image processing, the median plane of each wall. As for the volumetric mesh presented above, the gray scale images must be binarized by thresholding. Then, each cell of the gaseous phase has to be labeled. Each label can then be dilated isotropically through the solid phase until it encounters the neighboring dilating label (this procedure could be envisioned as a growing bubble procedure). At the end of this dilation procedure, the solid phase has been eliminated and the boundary between two neighboring labels lies exactly in the middle of the previously existing wall separating these two cells. As for the volumetric mesh again, the boundary between labels can be meshed using surface (shell) triangular elements and can be simplified to reduce the number of triangles while preserving a good description of the surface. A 3-D rendering of the shell surface mesh obtained after treating the binary image of Fig. 2a is illustrated in Fig. 2d.

In this type of meshing, homogeneous thicknesses can be allocated to all of the surface elements which are assumed to be plane parallel. In our study, the thicknesses of the faces adjacent to each element are adjusted so that the porosity of the reconstructed material equals the porosity of the real foam. In certain high-porosity closed-cell foams, the thicknesses of the cell faces are not constant along their areas but are slightly smaller at their centers in comparison with their borders (near the edges of cells). In this case, it is possible to take into account this difference in the shell mesh by attaching an individual thickness to each surface element. This has been done in [19]. The thickness of each surface element corresponds to the number of consecutive solid voxels in the normal direction of the element.

B. Computation of the Radiative Properties by Ray Tracing

In our model, the two different types of meshing described previously (volumetric surface mesh and shell surface mesh) have been used to compute the spectral radiative properties. As explained, the methods of computation of these properties are based on ray-tracing procedures inside the meshed volume.

1. Computation from the Volumetric Surface Mesh

Two ray-tracing procedures are required for the computations of the radiative properties from the volumetric surface mesh: one for the extinction coefficient and one for the scattering properties.

a. Extinction Coefficient β_λ. For the determination of the equivalent extinction coefficient, the principle is to compute the mean free path l_{mean} of the photons in the material from their generation to their extinction by the porous structure. This mean free path is related to the extinction coefficient of the equivalent semitransparent medium [15,16]:

$$\beta_\lambda = \frac{1}{\boldsymbol{l}_{\text{mean}}} \tag{6}$$

To compute the mean free path, we generate rays starting from random locations of the solid–fluid interface with random directions in the outward facing hemisphere of the interface (see Fig. 3). Ray paths are tracked until they encounter the solid phase, which will reflect, absorb or refract them. For a large amount of rays generated, we can calculate the mean distance traveled by the rays before interaction which converges to the mean free path of phonons. It is interesting to note that, in the volumetric mesh approach, given that all of the rays impacting the solid phase are either absorbed or scattered, the mean free path only depends on the microstructure of the foam. Mean free path is therefore independent of the wavelength and of the optical properties of the solid phase.

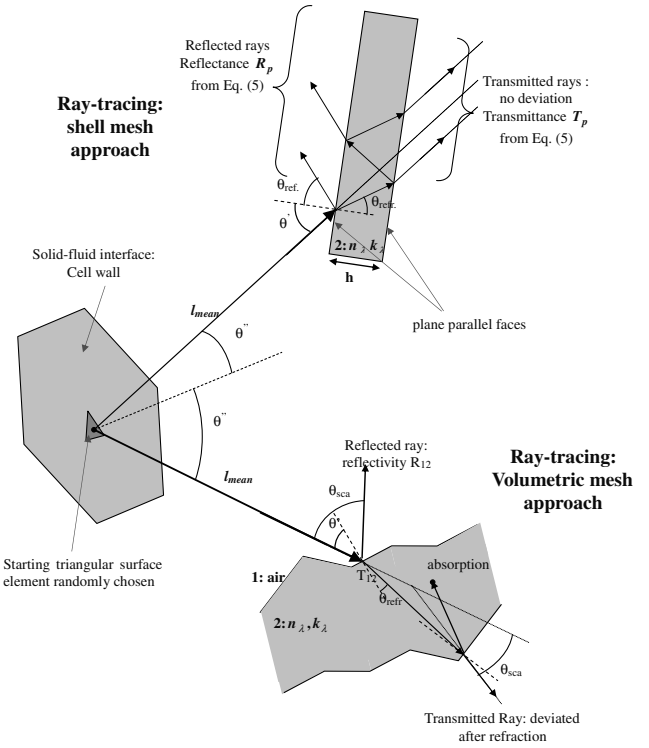

Fig. 3 Illustration of tomographic 3-D image of closed-cell foam at different levels.

In practice, for each ray, we randomly choose a triangular surface element of the mesh and a point of this element from which the ray starts (see Fig. 3). The random starting direction is chosen so that the angle between the starting direction and the outward normal of the element satisfies $\theta'' = \cos^{-1}(\xi)$, with ξ being a randomly generated number between 0 and 1. During the ray-tracing procedure, we also store the angles θ' between the rays and the normal to the surface elements impacted by the rays. Thus, we can compute the mean angular repartition of the rays impacting the solid phase, denoted by $E(\theta')$. In our method, the angular repartition is discretized for $\theta'_0 = 0°$, $\theta'_1 = 1°$, $\ldots$, $\theta_{180} = 180°$. Then, all of the rays impacting the solid phase with an angle between $\theta'_i - 0.5°$ and $\theta'_i + 0.5°$ are regrouped in $E(\theta'_i)$.

B. Scattering Albedo ω_λ *and Phase Function* $P_\lambda(\theta)$. The scattering albedo and phase function are computed by analyzing the paths of rays impacting the solid phase until they leave it. These rays can either be directly reflected, absorbed or scattered after one or several interactions with the solid phase (see Fig. 3). In practice, we follow the path of a large number of rays impacting the solid phase at random locations with random incident directions. Under the assumption of independent scattering, the probability that a ray impacts the solid phase with an incident angle comprised between θ' and $\theta' + \mathbf{d}\theta'$ to the normal of the solid phase is equal to $\sin\theta' \cos\theta' \mathbf{d}\theta'$. However, in our method, in order to take into account dependent scattering effects, we instead use the probability function given by the angular repartition of the incident angle $E(\theta'_i)$ obtained from the previous ray-tracing procedure for the extinction coefficient. The paths of the incident rays are tracked by computing the reflectivity of the fluid–solid interface. For plastic foams, these spectral reflectivities are obtained from the Fresnel relations [12–14] involving the refractive indexes of the solid phase and the incident angle.

The comparison of this reflectivity with a random number permits the determination of whether the ray enters the solid phase or is reflected and leaves directly. If the ray enters, its path is tracked until it reaches and crosses the solid–fluid interface again or until it is absorbed by the solid phase. For polymeric foams, absorption in the solid phase is dictated by the imaginary part of the refractive index, and the attenuation of the radiant energy follows Beer's law [12,14]:

$$\boldsymbol{I}_\lambda(z=\boldsymbol{l}) = \boldsymbol{I}_\lambda(z=0)\exp\left(-\frac{4\pi \boldsymbol{k}_\lambda}{\lambda}\boldsymbol{l}\right) \tag{7}$$

The ray-tracing procedure permits counting the number of rays which are absorbed ($\boldsymbol{N}_{\text{abs}}$), directly reflected ($\boldsymbol{N}_{\text{ref}}$) or scattered after several refractions and/or reflections in the solid phase ($\boldsymbol{N}_{\text{refr}}$). Each time a ray leaves the solid phase (after direct reflection or after refraction), the procedure stores the angle θ between its incident and departing directions. In this manner, we can compute the mean angular repartition of the radiative energy scattered by the solid phase, denoted as $D_\lambda(\theta_i)$ with $i = 0, 180$.

For a large number of rays $\boldsymbol{N}$, the scattering albedo can be evaluated by

$$\omega_\lambda = \left(\frac{\boldsymbol{N}-\boldsymbol{N}_{\text{abs}}}{\boldsymbol{N}}\right)_\lambda \tag{8}$$

The scattering phase function is obtained from the angular repartition $\boldsymbol{D}_\lambda(\boldsymbol{\theta}_i)$ which actually represents the probability for an incident ray to be scattered by the solid phase in a direction making an angle between $\theta_i - 0.5°$ and $\theta_i + 0.5°$ with the incident direction. On the other hand, $\frac{1}{4\pi}\boldsymbol{P}_\lambda(\theta_i)\,\mathbf{d\Omega}(\theta_i)$ represents the probability for the incident ray to be scattered in the solid angle $\mathbf{d\Omega}(\theta_i)$ centered on the direction θ_i. We then have

$$\begin{aligned}
&\boldsymbol{P}_\lambda(\theta_i) = 4\pi \boldsymbol{D}_\lambda(\theta_i)/\mathbf{d\Omega}(\theta_i) \quad \text{for } i = 0, 180\\
&\text{with } \mathbf{d\Omega}(\theta_i) = 2\pi\sin(\theta_i)\boldsymbol{\Delta}\theta_i = 2\pi\sin(\theta_i)\frac{2\pi}{360} \quad \text{for } i = 0, 180\\
&\text{so } \boldsymbol{P}_\lambda(\theta_i) = \frac{2\boldsymbol{D}_\lambda(\theta_i)}{\sin(\theta_i)\frac{\pi}{360}}
\end{aligned} \tag{9}$$

Thereafter, the phase function is normalized as

$$\frac{1}{2}\sum_{i=0}^{180}\boldsymbol{P}_\lambda(\theta_i)\sin(\theta_i)\,\mathbf{d}\theta_i = 1 \tag{10}$$

The method presented is applicable to porous materials whose radiative behavior can be approximated satisfactorily by an equivalent homogeneous and isotropic semitransparent medium. However, certain cellular materials present an anisotropic structure that may be due, for instance, to a difference in the expansion velocity during the foaming process. Our method also gives the opportunity to evaluate the degree of anisotropy of these materials by computing directional radiative properties. The principle of the numerical computation is identical to the one presented for the isotropic radiative properties except that the starting directions of the rays generated for the computation of the extinction coefficient are no more randomly chosen but correspond to the directions in which the radiative properties should be evaluated. Similarly, the incident directions of the rays impacting the solid phase for the computation of the scattering properties are no more chosen from the angular repartition $E(\theta')$ but correspond to the directions investigated.

2. *Computation from the Shell Surface Mesh*

As explained previously, for certain high-porosity closed-cell foams, the use of a shell surface mesh may be appropriate for the description of their porous structures. As for computations from the volumetric mesh, two different ray-tracing procedures are required: one for the mean free path and one for the scattering properties. The ray-tracing procedure for computing the mean free path is identical to the previous one (Sec. III.B.1). On the other hand, for the scattering properties, the Monte Carlo procedure is slightly different and simpler since the surface elements impacted by the rays are assumed to be plane parallel (see Fig. 3). Thus, it is not necessary to track the paths of the rays in the solid phase given that the total reflectance $\boldsymbol{R}_p$, absorbance $\boldsymbol{A}_p$, and transmittance $\boldsymbol{T}_p$ of the elements can be evaluated analytically from Eq. (5).

Therefore, the destiny of the rays (absorption, reflection or transmission) is determined using a randomly generated number which is compared with the magnitude of $\boldsymbol{A}_p$, $\boldsymbol{R}_p$ and $\boldsymbol{T}_p$. In this manner, the number of rays absorbed $\boldsymbol{N}_{\text{abs}}$, reflected $\boldsymbol{N}_{\text{ref}}$ or transmitted after refractions $\boldsymbol{N}_t$ are computed simply. It is interesting to note that, since the surface elements are considered plane parallel, the rays transmitted through the solid phase are not deviated from their incident directions regardless of their angles of incidence. Thus, transmitted rays continue as if they had not been intercepted by the solid phase. Consequently, the transmitted rays do not contribute to the extinction of the radiation and can be neglected. So, they should not be taken into account in the mean angular repartition of the radiative energy scattered by the solid phase $D'_\lambda(\theta_i)$. These differences from the volumetric mesh approach lead to modifications of the previous formulas expressing the corresponding extinction coefficient [Eq. (6)], scattering albedo [Eq. (8)] and scattering phase function [Eq. (9)]. For the shell-mesh approach, we have

$$\beta_\lambda = \frac{1}{\boldsymbol{l}_{\text{mean}}}\left(\frac{\boldsymbol{N}-\boldsymbol{N}_t}{\boldsymbol{N}}\right)_\lambda; \qquad \omega_\lambda = \left(\frac{\boldsymbol{N}_{\text{ref}}}{\boldsymbol{N}_{\text{abs}}+\boldsymbol{N}_{\text{ref}}}\right)_\lambda \tag{11}$$

$$\boldsymbol{P}_\lambda(\theta_i) = \frac{\boldsymbol{D}'_\lambda(\theta_i)}{\sin(\theta_i)\frac{\pi^2}{90}} \tag{12}$$

with

$$\frac{1}{2}\sum_{i=0}^{180}\boldsymbol{P}'_\lambda(\theta_i)\sin(\theta_i)\,\mathbf{d}\theta_i = 1$$

One can remark that, contrary to the volumetric mesh approach, the extinction coefficient computed via the shell-mesh approach varies with the wavelength and with the optical properties of the solid phase. Indeed, the mean free path $\boldsymbol{l}_{\text{mean}}$ is still a characteristic length that only depends on the morphology of the porous structure. But, the proportion $(\frac{N-N_t}{N})_\lambda$ of incident rays intercepted by the solid phase, which was equal to unity in the volumetric mesh approach, now depends on the refractive index of the polymer via Eq. (5).

IV. Theoretical Results and Discussion

We have applied the theoretical computations of the spectral radiative properties of three polymeric foam samples using the volumetric mesh and the shell-mesh approaches. The results obtained have been compared with each other and with the properties given by models previously developed in the literature which are based on simplified representation of the porous morphology. The comparison of the results obtained permitted us to investigate the errors generated by the different hypotheses concerning the porous structures and/or the solution methods.

A. Optical Properties of the Solid Phase

The computations of the radiative properties have been conducted on 3-D representations of PVC foams. Nevertheless, in order to be able to compare the results obtained numerically for the different foam structures with the results of simplified models, all of the computations were conducted using the refractive indexes of polystyrene. Actually, the spectral variations of these indexes are known accurately in the wavelength range [5, 50 μm] from [5].

B. Characterization of the Cellular Materials Tomographied

Radiative property computations were conducted on three samples of polymeric closed-cell foams of dimensions $1.75 \times 1.75 \times 1.75$ mm^3, $1.25 \times 1.25 \times 1.25$ mm^3 and $2.1 \times 2.1 \times 2.1$ mm^3. The voxel sizes for the 3-D images reconstructed were 7 μm for samples 1 and 3 and 5 μm for sample 2. The volumetric mesh used was composed of 5×10^4 triangular elements for sample 1 and 1×10^5 elements for samples 2 and 3, while the shell meshes consist of 2×10^4 elements for the three foam samples. Therefore, the geometrical accuracy (i.e., the number of elements per surface area) was the same order of magnitude for the two types of mesh. For each

of the foam samples, we have evaluated the minimum size of the representative elementary volume (REV), which is a critical point for the concept of continuum in a porous medium. We used the approach of Petrash et al. [11]. Hence, we computed the porosities $\varepsilon_{\mathrm{CV}}$ in cubic volumes with increasing edge length centered on different points of the tomographied volumes. As the edge length increased, the porosities converged to the same value ε, regardless of the original point considered. The minimum size of a REV is defined as the minimum edge length beyond which the variations of $\varepsilon_{\mathrm{CV}}$ around ε can be considered negligible. For the three foam samples considered, we have found that these variations are lower than $\pm 0.5\%$ as soon as the edge length is greater than 0.5 mm (REV $= 0.12$ mm^3), regardless of the original point on which the cubic volumes are centered. The tomographied volumes considered were much greater than this REV and, thus, could be considered as representative.

The 3-D representations of the porous structure obtained from tomography allowed us to estimate the porosity and the distribution of cell sizes. The porosity was simply estimated from the density of the materials considered, knowing the density of the polymer. The distribution of cell sizes was evaluated from the distribution of the volumes of all cells present in the sample. The volume $\boldsymbol{V}_i$ of each of the cells was obtained during the bubble growth algorithm. From this volume, it was possible to estimate an equivalent diameter for each cell depending on the shape of ideal cells considered (sphere, cube, dodecahedron, or tetrakaidecahedron). Indeed, we have $\boldsymbol{D}_{\mathrm{cell},i} = 2[3\boldsymbol{V}_i/(4\pi)]^{1/3}$, $\boldsymbol{D}_{\mathrm{cell},i} = (\boldsymbol{V}_i)^{1/3}$, $\boldsymbol{D}_{\mathrm{cell},i} \approx (\boldsymbol{V}_i/0.427)^{1/3}$, and $\boldsymbol{D}_{\mathrm{cell},i} = (2\boldsymbol{V}_i)^{1/3}$ for spherical, cubic, dodecahedral, and tetrakaidecahedral cells, respectively. Thereafter, the distribution of equivalent cell diameters in the foam sample could be estimated by gathering the values obtained for each cell. The crucial morphological characteristics (porosity, number of cells, and distribution of equivalent cell diameters, etc.) of the three foam samples tomographied are summarized on Table 1. In this table, we indicate (for each foam sample) the mean equivalent diameter $\langle D_{\mathrm{cell}}\rangle$, the standard deviation of the cell diameters $\sigma_{D\mathrm{cell}}/\langle D_{\mathrm{cell}}\rangle$, and the equivalent diameter of the biggest (max.) and smallest (min.) cell. We only indicate the equivalent spherical diameters given that the corresponding equivalent diameters for a cube, dodecahedron, and tetrakaidecahedron can be obtained from the previous relations between D_{cell} and V.

C. Analysis

For the two types of meshes considered, ray-tracing procedures have been carried out with $\boldsymbol{N} = 1 \times 10^5$ rays for the computation of the mean free paths and $\boldsymbol{N} = 1 \times 10^6$ incident rays for the computations of the scattering properties. The computation of the scattering properties had to be conducted for every wavelength analyzed. In our study, we considered a total of 180 wavelengths in the range $[5, 50]$ μm. The computations have been carried out on a PC with the following characteristics: Intel Core 2 Quad CPU, 2.67 GHz, 1.98 gigaoctets of RAM. The computation of the mean free paths required less than 1 h for the volumetric and shell mesh while the computation of the scattering properties for all the wavelengths required between 1 and 3 h for the volumetric mesh and only few minutes for the shell mesh. We have checked the isotropy of the three foam samples tested by computing the extinction coefficients β_X, β_Y, and β_Z in the three orthogonal directions X, Y, and Z and the homogeneous equivalent extinction coefficient β_{random} in random directions. The relative differences

$$(\boldsymbol{\Delta}\beta/\beta)_{X/Y/Z} = (\beta_{X/Y/Z} - \beta_{\mathrm{random}})/\beta_{\mathrm{random}}$$

in the different directions were $(\frac{\boldsymbol{\Delta}\beta}{\beta})_{X/Y/Z} = -9\%$, -1.7%, and -0.9% for sample 1; $(\frac{\boldsymbol{\Delta}\beta}{\beta})_{X/Y/Z} = -2.1\%$, -4.1%, and -5.5% for sample 2; and $(\frac{\boldsymbol{\Delta}\beta}{\beta})_{X/Y/Z} = -2.1\%$, -1.3%, and -3.8% for sample 3. Therefore, the hypothesis of isotropic semitransparent material was assumed to be valid.

1. Improvements Brought by the Shell-Mesh Computation

The shell-mesh approach models the solid phase as a connection of plane-parallel surface elements to which individual thicknesses are allocated (see Sec. III.A).

In addition to the shell-mesh computation, we have also applied the prior simplified models of [5] assuming ideal shapes of cells (cubic, dodecahedral, and tetrakaidecahedral) to the three foam samples. However, instead of considering a single cell size, as in [5] (corresponding to the mean cell size of the sample for example), we have taken into account the cell-size distribution in the sample by averaging the radiative properties computed by the ideal-cell model [5] over the total number of cells. Two different types of averaging were considered:

1) The first type was a simple arithmetic averaging:

$$\beta_{\mathrm{av1},\lambda} = \frac{\sum_{i=1,N\mathrm{cell}} \beta_\lambda(\boldsymbol{D}_{\mathrm{cell},i})}{\boldsymbol{N}_{\mathrm{cell}}}; \qquad \omega_{\mathrm{av1},\lambda} = \frac{\sum_{i=1,N\mathrm{cell}} \omega_\lambda(\boldsymbol{D}_{\mathrm{cell},i})}{\boldsymbol{N}_{\mathrm{cell}}} \tag{13}$$

2) The second type was an averaging weighted by the volume of each cell:

$$\beta_{\mathrm{av2},\lambda} = \frac{\sum_{i=1,N\mathrm{cell}} \beta_\lambda(\boldsymbol{D}_{\mathrm{cell},i})\boldsymbol{V}_i}{\sum_{i=1,N\mathrm{cell}} \boldsymbol{V}_i}; \qquad \omega_{\mathrm{av2},\lambda} = \frac{\sum_{i=1,N\mathrm{cell}} \omega_\lambda(\boldsymbol{D}_{\mathrm{cell},i})\boldsymbol{V}_i}{\sum_{i=1,N\mathrm{cell}} \boldsymbol{V}_i} \tag{14}$$

In this averaging, the large cells of the sample, which occupy a greater volume, have a greater influence on the radiative properties of the foam.

The comparison between the results of the shell-mesh computation and of the simplified models stemming from the prior study [5] permitted us to quantify the error generated when the shape and/or the size of the cells are assumed to be regular and homogeneous. Indeed, the results of the shell-mesh approach could be considered as a baseline since it used the same hypotheses as the ideal-cell models of [5] (plane-parallel windows) but took into account dependent scattering effects and the real morphology of the samples (irregular shapes of the cells, variation in wall thickness, variation in cell size). The comparisons are illustrated in Figs. 4–6 for samples 1, 2, and 3, respectively.

The comparison of the spectral radiative properties shows important differences among the models. For the extinction coefficient, the trends in the spectral variations are quite similar for all of the models, but the values computed are noticeably different.

First of all, the extinction coefficients obtained by the ideal-cell models [5] with arithmetic averaging (AV1) are always greater than the ones computed from volumetric averaging (AV2). This can be explained by the fact that, in AV2, a greater influence is allocated to the large cells of the sample for which the extinction coefficient is lower (the mean free path is longer in these cells). As expected, the differences between the two averaging methods are relatively weak for the sample in which the distribution of cell sizes is narrow (sample 2, $\frac{\sigma_{D\mathrm{cell}}}{\langle \boldsymbol{D}_{\mathrm{cell}}\rangle} = 0.16$) whereas the type of averaging technique could be very important for samples exhibiting a wide distribution of cell sizes (sample 3, $\frac{\sigma_{D\mathrm{cell}}}{\langle \boldsymbol{D}_{\mathrm{cell}}\rangle} = 0.65$). The shape of the ideal cells

Table 1 Summary of the morphological characteristics of the three foam samples tomographied

Sample no.	$\boldsymbol{N}_{\mathrm{cell}}$	ε	$\langle \boldsymbol{D}_{\mathrm{cell,sphere}}\rangle$, μm	$\frac{\sigma_{D\mathrm{cell}}}{\langle \boldsymbol{D}_{\mathrm{cell}}\rangle}$	Max. $\boldsymbol{D}_{\mathrm{cell,sphere}}$, μm	Min. $\boldsymbol{D}_{\mathrm{cell,sphere}}$, μm
1	31	0.943	372	0.495	627	64
2	50	0.907	296	0.16	379	215
3	39	0.957	326	0.653	803	41

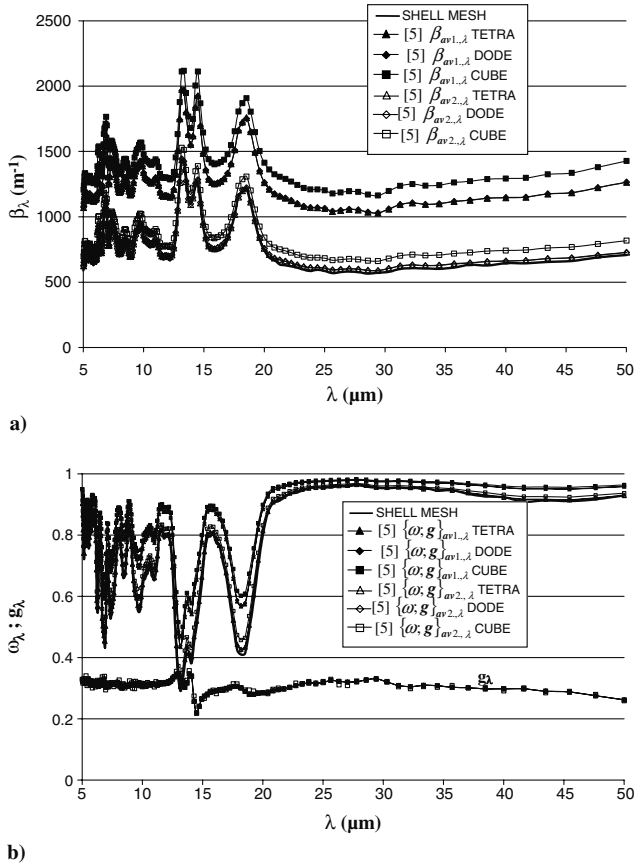

Fig. 4 Comparison of the radiative properties of sample 1, obtained from the tomographic shell mesh and the model of Coquard et al. [5] with cell-size distribution.

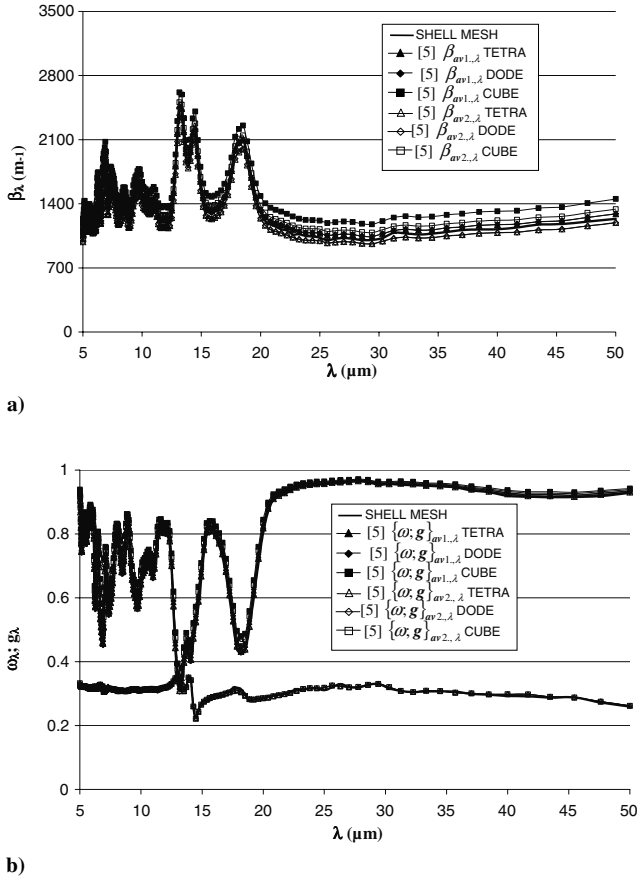

Fig. 5 Comparison of the radiative properties of sample 2, obtained from the tomographic shell mesh and the model of Coquard et al. [5] with cell-size distribution.

modeled has also an influence on the extinction coefficients since cubic cells always give greater extinction coefficients than dodecahedron or tetrakaidecahedron cells (which are almost identical in all the cases considered). The relative differences between cubic and dodecahedral/tetrakaidecahedral shapes are practically the same regardless of the sample and the averaging method considered and are close to 10%.

Second, we can notice that, for the three samples, the ideal-cell models of [5] with AV2 give results much closer to the shell-mesh approach than when AV1 is considered. Indeed, the mean relative differences between the shell-mesh approach and the ideal-cell models for samples 1, 2, and 3 (averaged over the wavelength range $[5, 50]$ μm) are as follows:

1) The first mean relative differences are +5.3%, +4.8%, and +11% for volume averaging with dodecahedron/tetrakaidecahedron cells.

2) The second mean relative differences are +13.7%, +12.3%, and +22.8% for volume averaging with cubic cells.

3) The third mean relative differences are +65%, +1.8%, and +195% for AV1 with dodecahedron/tetrakaidecahedron cells.

4) The fourth mean relative differences are +84%, +12.3%, and +227% for AV1 with cubic cells

It is interesting to remark that the results of the ideal-cell models always overestimate the extinction coefficients given by the shell-mesh approach regardless of the sample (1, 2, and 3), the cell shape (cube and dodecahedron/tetrakaidecahedron) or the averaging method (AV1 and AV2). The results clearly show that the ideal-cell model with dodecahedron/tetrakaidecahedron cells and AV2 is the most suitable for predicting the radiative behavior of polymer closed-cell foams. The errors made with this model are relatively weak and might be acceptable in most studies concerned with the predictions of radiative heat fluxes. The use of cubic cells for the ideal-cell model with AV2 leads to noticeably larger differences. We can also conclude from these comparisons that simple AV1 is definitely not suitable for the prediction of the extinction coefficient. Indeed, it leads to very important errors especially for samples with a wide cell-size distribution (samples 1 and 3). However, one can notice a surprising result for sample 2, since the extinction coefficients given by the ideal-cell model with dodecahedron/tetrakaidecahedron cells and AV1 are the closest to the shell-mesh approach (mean difference = 1.8%). This can be explained by the fact that the cell-size distribution in this sample is very narrow (see Table 1), so that the arithmetic and AV2 lead to almost identical extinction coefficients (see Fig. 5). Besides, the ideal-cell model with dodecahedron/tetrakaidecahedron cells and AV2 gives also satisfactory predictions (mean difference = 4.8%). So, the appropriateness of the models should be preferably assessed on samples with wide cell-size distributions.

As regards the scattering albedo, the trends in the spectral variations predicted are quite similar for all of the models (ideal cell or shell mesh). But the absolute values can differ significantly. The ideal-cell models overestimate the scattering albedo for the whole radiation spectrum regardless of the foam sample or the cell shape. Globally, we remark that the cubic shape leads to greater albedos than dodecahedron/tetrakaidecahedron cells. We also notice that, as for the extinction coefficient, the results with AV1 are noticeably different from the results of the shell-mesh approach, especially for the foam sample with a wide cell-size distribution (sample 3). On the other hand, the ideal-cell models with AV2 give much more satisfying results. Indeed, the mean relative differences between the albedos predicted by these models assuming dodecahedral/tetrakaidecahedral cells and the shell-mesh results are lower than 5, 1.5, and 4% for foam samples 1, 2, and 3, respectively, over the whole wavelength range.

Finally, the scattering phase functions predicted by all of the different models assuming plane-parallel windows (ideal-cell models and the shell-mesh model) are almost identical regardless of the wavelength. Moreover, they are also practically identical for the

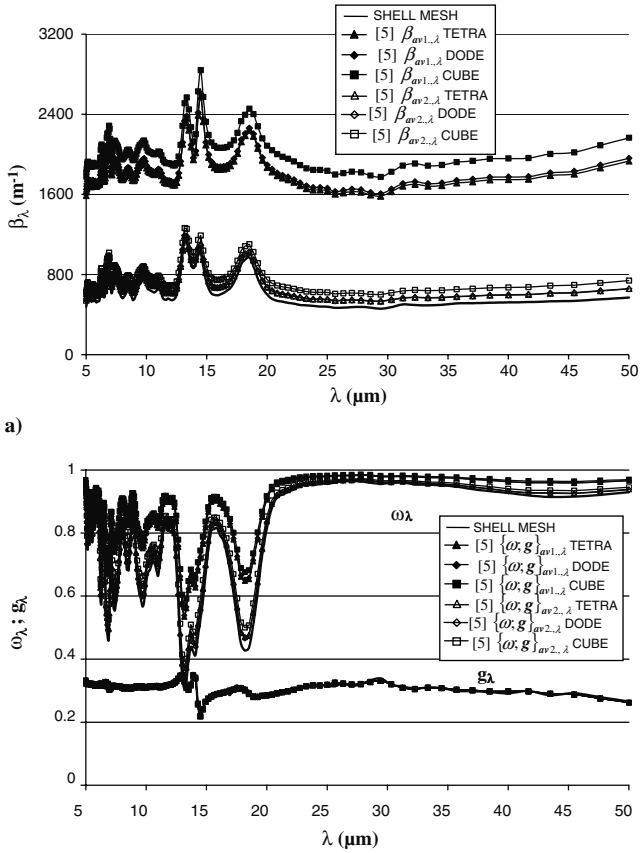

Fig. 6 Comparison of the radiative properties of sample 3, obtained from the tomographic shell mesh and the model of Coquard et al. [5] with cell-size distribution.

three foam samples, although their structural characteristics and densities are quite different. This is illustrated in Fig. 7 for the radiation wavelength $\lambda = 10\ \mu$m. One can notice that when the cell windows are assumed to be plane parallel, the scattering by the cellular materials is predominantly oriented in the forward direction regardless of the wavelength considered ($g_\lambda > 0$). Actually, given that the solid phase of any polymeric foam could be considered as a dielectric ($k_\lambda \ll n_\lambda$), this conclusion is valid regardless of the type of plastic foam (polystyrene, PVC, PU, etc.).

In summary, it appears that ideal-cell models with dodecahedron/tetrakaidecahedron cells and AV2 permits the prediction of radiative properties which are very close to the baseline shell-mesh approach for the whole wavelength range and for all the samples considered. Therefore, this model may be used to estimate satisfactorily the radiative behavior of polymer foams. On the other hand, the ideal-cell models with AV1 or which consider cubic cells are not able to fit these properties satisfactorily.

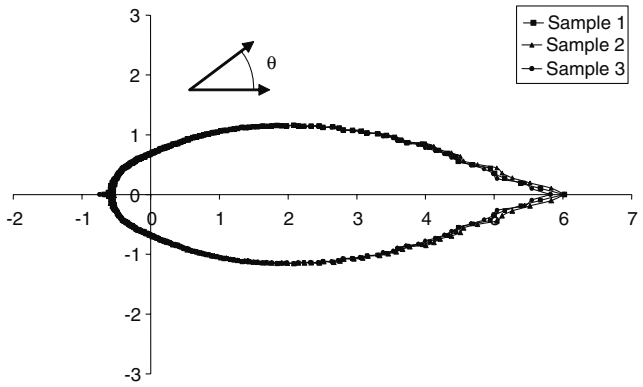

Fig. 7 Illustration of the scattering phase functions computed from the shell-mesh approach at $\lambda = 10\ \mu$m for the three foam samples.

The slight differences observed between the spectral extinction coefficients and scattering albedos computed by the ideal-cell models with dodecahedron/tetrakaidecahedron cells and AV2 versus those computed by the shell-mesh approach may be explained by several reasons:

1) The ideal shapes of cells considered (dodecahedron/tetrakaidecahedron) are not really representative of the cells encountered in the real porous structure.

2) The variation of cell size in the real porous structure leads to variation in the repartition of the solid phase in the windows, which is not accurately reproduced by the ideal-cell structures, which assume a constant wall thickness.

3) The variation in the thicknesses of the windows is neglected in the ideal-cell models.

4) The independent scattering regime assumed in the ideal-cell models might not be fully valid for the foam samples studied. Therefore, dependent scattering effects that are taken into account in the shell-mesh approach could lead to substantial differences.

As a conclusion, we have managed to show that the ideal-cell models with dodecahedron/tetrakaidecahedron cells and AV2 are the most suitable to predict the radiative behavior of closed-cell foams composed of plane-parallel walls. However, the use of tomographic analysis via shell meshing is interesting for estimating these properties with a higher level of accuracy as it overcomes the deficiencies of the ideal-cell models. Thus, shell meshing constitutes a noticeable improvement in the field of radiative properties modeling.

2. *Improvements Produced by the Volumetric Mesh Computations*

As explained in the previous paragraph, the shell-mesh approach permits improvement of the modeling of radiative properties of closed-cell foams as it takes into account more faithfully their real porous structures. However, it is based on a strong hypothesis concerning the structure of the foams and the radiation-matter interaction, since the cell windows are assumed (locally) to be plane

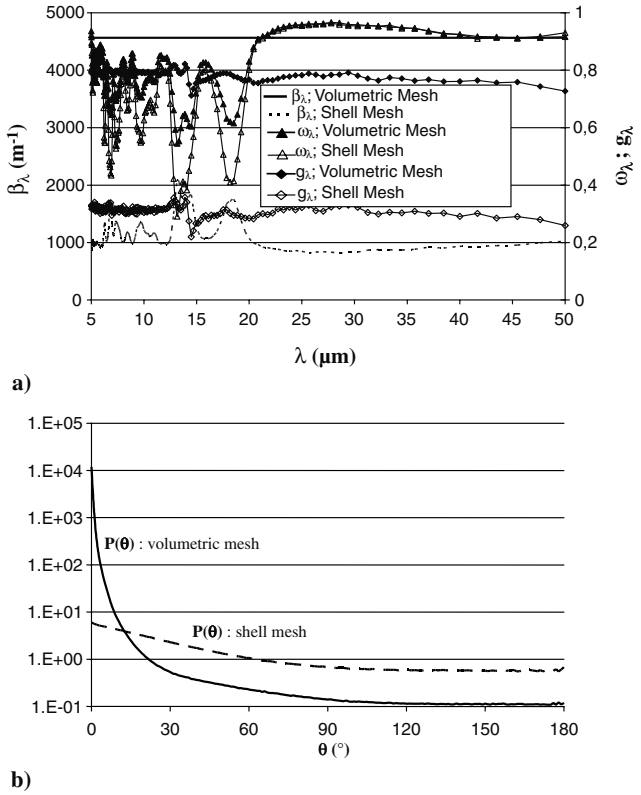

Fig. 8 Comparison of the spectral radiative properties computed from shell-mesh and volumetric mesh approaches for sample 1.

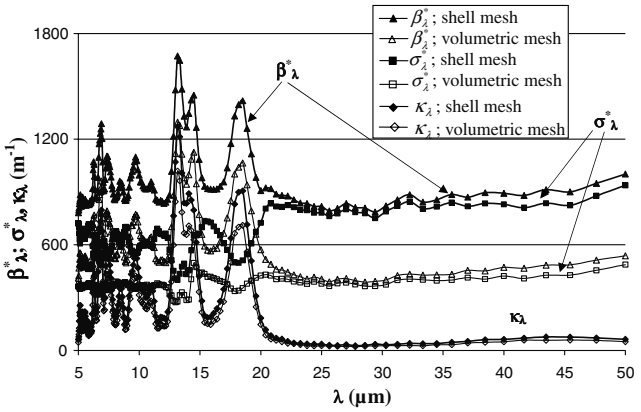

Fig. 9 Comparison of the spectral absorption coefficients and weighted extinction coefficients of sample 1, obtained from the tomographic shell-mesh and volumetric mesh approaches.

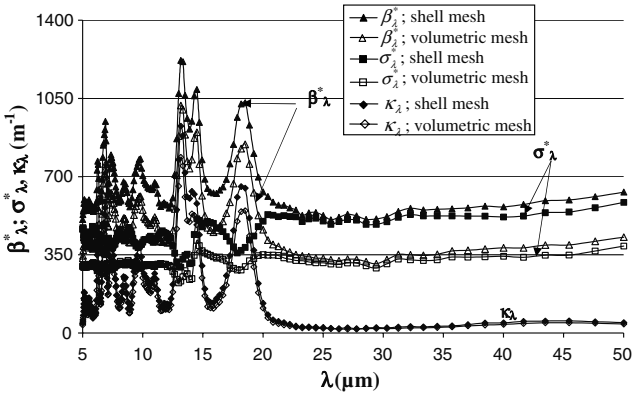

Fig. 11 Comparison of the spectral absorption coefficients and weighted extinction coefficients of sample 3, obtained from the tomographic shell-mesh and volumetric mesh approaches.

parallel. Thus, the radiation intensity refracted by the cell faces is treated as if it were not intercepted. In real porous structures, the boundaries of cell windows are not perfectly parallel to each other, even for very highly porous foams for which the wall thickness is very low ($h \approx 1$ μm). As a consequence, the rays passing through the cell walls are deflected and thus the radiative energy is redirected. To evaluate the influence of this phenomenon, the volumetric surface mesh approach described in Sec. III.B.1 has been applied to the three foam samples. This takes into account more faithfully the local solid phase repartition.

The results obtained are compared using the radiative properties stemming from the shell-mesh approach in Fig. 8 for foam sample 1.

At first glance, the results obtained differ largely. This could lead one to believe that the radiative behavior predicted by the two approaches is totally different. Notably, it is surprising that the extinction coefficient computed from the volumetric surface approach is independent of the wavelength, since the results obtained previously with the shell-mesh approach show strong variation. However, one has to keep in mind that, in the volumetric mesh approach, all of the rays hitting the solid phase are either absorbed or scattered. Indeed, even the rays passing through the windows are redirected (see Fig. 3). Whereas, in the shell-mesh approach (as well as in ideal-cell models), the cell windows are assumed to be plane parallel or composed of plane-parallel surface elements so that the rays passing through the window elements are parallel to the incident direction (see Fig. 3). Thus, such rays are not considered to be intercepted by the solid phase and do not contribute to the extinction coefficient. This leads to noticeably higher values of the extinction coefficient in the volumetric mesh approach (Fig. 8a) and to a scattering phase function much more oriented in the forward direction (Fig. 8b). However, these differences do not necessarily imply that the radiative behavior predicted by the two approaches is noticeably different. In actuality, the radiative behavior predicted by the two approaches may be globally similar. Therefore, it seems judicious to resort to radiative parameters more relevant to the comparison between the two approaches such as the absorption coefficient κ_λ, the weighted scattering coefficient σ^*_λ and the weighted extinction coefficient β^*_λ defined before [Eq. (3)].

Actually, as explained in Sec. II, σ^*_λ encompasses the whole scattering phenomenon. For example, semitransparent media in which the scattering events only lead to slight deflections of the radiative energy (asymmetry parameter g_λ close to one) have a lower value of σ^*_λ than materials whose porous structures strongly backscatter the incident radiation. On the other hand, the absorption coefficient κ_λ does not involve any redirection phenomenon and thus, has the same significance in both approaches (shell mesh and volumetric mesh). The spectral variations of the weighted radiative properties computed by the two approaches are illustrated on Figs. 9–11. We also report, in Table 2, the global values of the weighted coefficients computed by the two approaches for a blackbody temperature $T = 300$ K [see Eq. (4)].

Comparison of the weighted radiative properties indicates that the radiative behavior predicted by the volumetric mesh and shell-mesh approaches exhibit important differences. The absorption coefficients obtained by the two approaches are very close to each other for the whole wavelength range. But, the weighted scattering coefficients and, consequently, the extinction coefficients stemming from the volumetric approach are noticeably greater than the ones computed from the shell-mesh approach. This is in good agreement with the previous remarks given, that the magnitude of absorption which mainly depends on the thickness of the cell windows has no reason to be greater in one approach as compared with the other. On the other hand, we have seen previously that, in the volumetric approach, the deviation of the radiative energy passing through the cell windows enhances the scattering phenomenon resulting in an increase in the weighted scattering coefficient. However, considering Fig. 2b, which shows nearly plane-parallel cell windows, one would have thought that the amount of scattering due to the deviation of rays transmitted through the cell faces might be relatively small. The calculations indicate that this effect is, in fact, substantial. For the foams studied, it appears that neglecting the radiation scattered due to refraction in the cell windows by assuming plane-parallel faces could lead to significant errors. It is also interesting to notice that the enhancement of scattering by refraction inside the cell windows is not the same magnitude for all of the foam samples. Indeed, it is noticeably more pronounced for samples 1 (+42% for σ^*_λ) and 2 (+50.4%) than for sample 3 (+29.7%). This can be explained by the fact that samples 1 and 2 have noticeably lower porosities than sample 3. Therefore, they are composed of relatively thick cell windows so that their porous morphology is not well represented by shell meshing. On the other hand, sample 3, which is highly porous, has relatively thin cell windows, and its microstructure is better matched by shell meshing.

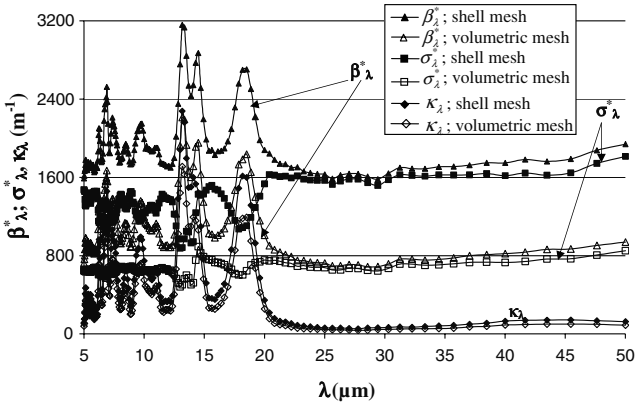

Fig. 10 Comparison of the spectral absorption coefficients and weighted extinction coefficients of sample 2, obtained from the tomographic shell-mesh and volumetric mesh approaches.

Table 2 Illustration of the global radiative properties computed by the shell-mesh and volumetric mesh approaches for the three foam samples

Foam sample	Model	κ, m^{-1}	σ^*, m^{-1}	β^*, m^{-1}	$\frac{\kappa_{VM}-\kappa_{SM}}{\kappa_{SM}}$, %	$\frac{\sigma^*_{VM}-\sigma^*_{SM}}{\sigma^*_{SM}}$, %	$\frac{\beta^*_{VM}-\beta^*_{SM}}{\beta^*_{SM}}$, %
1	Shell mesh	272.7	375.6	648.3	+7.3	+42.2	+31.2
	Volumetric mesh	292.6	649.9	942.5			
2	Shell mesh	464.9	669.1	1134	+13.1	+50.4	+39.6
	Volumetric mesh	525.8	1351	1876.8			
3	Shell mesh	208.3	310.3	518.7	+5.4	+29.7	+21.5
	Volumetric mesh	219.5	441.4	660.9			

Nevertheless, it appears that the shell-mesh approach could not be considered as very accurate, even for sample 3, since a relative difference of 21.5% is found with the volumetric shell approach. The latter can be considered the more detailed and accurate approach.

V. Conclusions

In this study, and for the first time, x-ray tomography has been used for the prediction of the radiative properties of closed-cell foams. The spectral extinction coefficients, scattering albedo and scattering phase function have been computed from ray-tracing procedures in 3-D mesh representing the real cellular structures of several polymeric foams. Two types of meshing of the solid phase have been investigated: the shell mesh assuming that the polymer is entirely composed of plane-parallel cell windows and the volumetric mesh which takes into account the cellular structure tomographied without any simplification.

First, we have compared, for three different foam samples, the radiative properties computed by the shell-mesh approach with the results stemming from theoretical models from the literature which also use the hypothesis of plane-parallel cell windows. These models are based on ideal representations of the cellular structure (cube, dodecahedron or tetrakaidecahedron with homogeneous repartition of the solid phase in cell windows) and assume independent scattering by the particles forming the material. The comparison permitted us to evaluate the influence of the dependent scattering phenomenon as well as the influence of the simplifications of the cellular shape (cubic, dodecahedral, or tetrakaidecahedral cells), of the solid phase repartition (constant window thickness), and of the cell-size distribution on the accuracy of the computed radiative properties.

It appears that the ideal-cell models which take into account dodecahedral/tetrakaidecahedral cells and AV2 for the cell-size distribution satisfactorily predict the radiative behavior of the foams computed by the shell-mesh approach. The relative differences are lower than 10% for the three foam samples investigated. The other ideal-cell models fail to predict accurately the extinction coefficients and scattering albedos. The present shell-mesh approach constitutes a noticeable improvement over the prior models, since it permits us to evaluate the reliability of the prior simplified models.

Thereafter, we have compared the weighted radiative properties computed using the two types of meshing in order to evaluate the validity of the assumption of plane-parallel cell windows and the errors generated. It appears that this hypothesis leads to a significant underestimation of the radiation scattered by the porous structure for the foam samples studied, whereas the spectral absorption coefficients are almost identical for the two approaches. Actually, the deviation of the radiative energy by refraction of the rays passing through cell windows is significant for the foam samples tested and leads to a noticeable underestimation of the weighted extinction coefficient when the shell-mesh approach is used. However, the differences between the two types of modeling become less important when the porosity of the sample increases. This can be explained by the fact that when the porosity increases, the thicknesses of cell windows decrease and the variation of the thicknesses between their centers and their borders decrease. Therefore, they become closer to thin plane-parallel plates. It would be interesting to conduct a similar study on plastic foams with higher porosities in order to determine for which porosity levels the errors caused by the plane-parallel approximation could be considered to be negligible.

Acknowledgment

This study is a part of the French ANRMatetPro-08-34-5476 project entitled THOMMI, which has been financed by the Agence Nationale de la Recherche from 2009 to 2011.

References

[1] Glicksmann, L. R., and Schuetz, M. A., "Radiation Heat Transfer in Foam Insulation," *International Journal of Heat and Mass Transfer*, Vol. 30, No. 1, 1987, pp. 187–197. doi:10.1016/0017-9310(87)90071-8

[2] Kuhn, J., Ebert, H. P., Arduini Schuster, M. C., Buttner, D., and Fricke, J., "Thermal Transport in Polystyrene and Polyurethanes Foam Insulations," *International Journal of Heat and Mass Transfer*, Vol. 35, No. 7, 1992, pp. 1795–1801. doi:10.1016/0017-9310(92)90150-Q

[3] Kuhn, J., Placido, E., and Arduini Schuster, M. C., "Thermal Properties Predictive Model for Insulating Foams," *Infrared Physics and Technology*, Vol. 46, No. 3, 2005, pp. 219–231. doi:10.1016/j.infrared.2004.04.001

[4] Coquard, R., and Baillis, D., "Modeling of Heat Transfer in Low-Density Expanded Polystyrene Foams," *Journal of Heat Transfer*, Vol. 128, No. 6, 2006, pp. 538–549. doi:10.1115/1.2188464

[5] Coquard, R., Baillis, D., and Quenard, D., "Radiative Properties of Expanded Polystyrene Foams," *Journal of Heat Transfer*, Vol. 131, No. 1, 2009, Paper 012702. doi:10.1115/1.2994764

[6] Loretz, M., Maire, E., and Baillis, D., "Analytical Modeling of the Radiative Properties of Metallic Foams: Contribution of X-Ray Tomography," *Advanced Engineering Materials*, Vol. 10, No. 4, 2008, pp. 352–360. doi:10.1002/adem.200700334

[7] Zeghondy, B., Iacona, E., and Taine, J., "Determination of the Anisotropic Radiative Properties of a Porous Material by Radiative Distribution Function Identification (RDFI)," *International Journal of Heat and Mass Transfer*, Vol. 49, Nos. 17–18, 2006, pp. 2810–2819. doi:10.1016/j.ijheatmasstransfer.2006.02.034

[8] Zeghondy, B., Iacona, E., and Taine, J., "Experimental and RDFI Calculated Radiative Properties of a Mullite Foam," *International Journal of Heat and Mass Transfer*, Vol. 49, Nos. 19–20, 2006, pp. 3702–3707. doi:10.1016/j.ijheatmasstransfer.2006.02.036

[9] Tancrez, M., and Taine, J., "Direct Identification of Absorption and Scattering Coefficients and Phase Function of a Porous Medium by a Monte Carlo Technique," *International Journal of Heat and Mass Transfer*, Vol. 47, No. 2, 2004, pp. 373–383. doi:10.1016/S0017-9310(03)00146-7

[10] Rousseau, B., Di Michiel, M., Canizares, A., De Sousa Meneses, D., Echegut, P., and Thovert, J. F., "Temperature Effect (300–1500 K) on the Infrared Photon Transport Inside an X-Ray Microtomographic Reconstructed Porous Silica Glass," *Journal of Quantitative Spectroscopy and Radiative Transfer*, Vol. 104, No. 2, 2007, pp. 257–265. doi:10.1016/j.jqsrt.2006.07.015

[11] Petrasch, J., Wyss, P., and Steinfeld, A., "Tomography-Based Monte Carlo Determination of Radiative Properties of Reticulate Porous Ceramics," *Journal of Quantitative Spectroscopy and Radiative Transfer*, Vol. 105, No. 2, 2007, pp. 180–197.

doi:10.1016/j.jqsrt.2006.11.002
[12] Siegel, R., and Howell, J. R., *Thermal Radiation Heat Transfer*, 3rd ed., Hemisphere, Washington DC, 1992.
[13] Modest, M. F., *Radiative Heat Transfer*, McGraw–Hill, New York, 1993.
[14] Brewster, M. Q., *Thermal Radiative Transfer and Properties*, Wiley, New York, 1992.
[15] Randrianalisoa, J., and Baillis, D., "Radiative Transfer in Dispersed Media: Comparison Between Homogeneous Phase and Multiphase Approaches," *Journal of Heat Transfer*, Vol. 132, No. 2, Feb. 2010 Paper 023405.
doi:10.1115/1.4000237
[16] Randrianalisoa, J., and Baillis, D., "Radiative Properties of Densely Packed Spheres in Semitransparent Media: A New Geometric Optics Approach," *Journal of Quantitative Spectroscopy and Radiative Transfer* (accepted for publication).
doi:10.1016/j.jqsrt.2010.01.014
[17] Maire, E., Buffière, J. Y., Salvo, L., Blandin, J. J., Ludwig, W., and Létang, J. M., "On the Application of X-Ray Microtomography in the Field of Materials Science," *Advanced Engineering Materials*, Vol. 3, No. 8, 2001, pp. 539–546.
doi:10.1002/1527-2648(200108)3:8<539::AID-ADEM539>3.0.CO;2-6
[18] Youssef, S., Maire, E., and Gaertner, R., "Finite Element Modelling of the Actual Structure of Cellular Materials Determined by X-Ray Tomography," *Acta Materialia*, Vol. 53, No. 3, Feb. 2005, pp. 719–730.
doi:10.1016/j.actamat.2004.10.024
[19] Caty, O., Maire, E., Youssef, S., and Bouchet, R., "Modeling the Properties of Closed-Cell Cellular Materials from Tomography Images Using Finite Shell Elements," *Acta Materialia*, Vol. 56, No. 19, Sept. 2008, pp. 5524–5534.
doi:10.1016/j.actamat.2008.07.023